nature materials

LETTERS

PUBLISHED ONLINE: 26 FEBRUARY 2012 | DOI: 10.1038/NMAT3256

Gated three-terminal device architecture to eliminate persistent photoconductivity in oxide semiconductor photosensor arrays

Sanghun Jeon[1]*, Seung-Eon Ahn[1], Ihun Song[1]*, Chang Jung Kim[1], U-In Chung[1], Eunha Lee[2], Inkyung Yoo[1], Arokia Nathan[3], Sungsik Lee[4], John Robertson[3] and Kinam Kim[1]

The composition of amorphous oxide semiconductors, which are well known for their optical transparency[1–4], can be tailored to enhance their absorption and induce photoconductivity for irradiation with green, and shorter wavelength light. In principle, amorphous oxide semiconductor-based thin-film photoconductors could hence be applied as photosensors. However, their photoconductivity persists for hours after illumination has been removed[5,6], which severely degrades the response time and the frame rate of oxide-based sensor arrays. We have solved the problem of persistent photoconductivity (PPC) by developing a gated amorphous oxide semiconductor photo thin-film transistor (photo-TFT) that can provide direct control over the position of the Fermi level in the active layer. Applying a short-duration (10 ns) voltage pulse to these devices induces electron accumulation and accelerates their recombination with ionized oxygen vacancy sites, which are thought to cause PPC. We have integrated these photo-TFTs in a transparent active-matrix photosensor array that can be operated at high frame rates and that has potential applications in contact-free interactive displays.

The oxide semiconductor TFT is a leading candidate for the next generation of large-area electronic systems, as it can be deposited at low temperature with high uniformity over large areas[1–4,7–12], showing high mobility ($\sim$30 $cm^2 s^{-1}V^{-1}$), low sub-threshold slope ($\sim$0.1 V/dec) and high bias stability, even when deposited at low temperatures[1–4,7–10]. These attributes have triggered intensive research on oxide semiconductors and, in particular, the In–Zn–O (IZO) and Ga–In–Zn–O (GIZO) systems[1,2,7,9,10,13].

Despite the advantages of the metal oxide semiconductor materials system for transistors, and in particular, active-matrix large-area imaging arrays, the oxide semiconductor TFT has a critical drawback associated with oxygen vacancies located within the bandgap[14,15], leading to persistent photoconductivity (PPC; refs 5,6,13–15), especially under short-wavelength light[16,17]. PPC causes the semiconductor material to remain conductive for hours/days, even in the absence of light[15–17]. This increases the response times and limits the frame rates. Although a variety of optical sensors using oxide semiconductors have been reported, they are generally two-terminal devices[17,18], and such configurations do not allow rapid recovery from the effects of PPC (refs 16–18).

To eliminate PPC rapidly and intentionally, a three-terminal device structure (that is, a gated TFT or photo-TFT) is employed in the pixel area with an appropriate bias scheme. Photo-TFTs provide the necessary control over the position of the Fermi level to enable the implementation of an operational scheme to manage the PPC problem[19–21]. This involves applying a short (10 ns), positive gate voltage pulse, which erases the PPC by inducing electron accumulation; this is thought to accelerate the recombination of electrons with ionized oxygen vacancy sites, which are believed to be the origin of the PPC problem. This operating scheme works despite the fact that the photo-TFTs are negatively biased to increase sensitivity during read-out. Unfortunately, this negative bias would act to compound the PPC by extending the recovery time to very large timescales if it were not controlled by the voltage pulse. Using this pulse operational scheme, we have fabricated a working all-TFT transparent photosensor array with a frame rate of 150 Hz.

Furthermore, the transparency associated with PPC is dependent on the wavelength of incident light. The perception of nano and thin-film oxide semiconductor structures being optically transparent is only true for large wavelengths, despite the wide bandgap of oxide semiconductors[22]. In fact, the absorption at short wavelengths has led to the development of two-terminal photosensors, such as photodiodes[23,24]. Although they are structurally simple[25,26], they are not process compatible with the switching TFTs used in the active matrix. More importantly, they are not able to provide any form of bias control over the photosensitivity of the device.

This work presents an all-oxide semiconductor three-terminal gated photosensor array in which the active channel consists of a stack of GIZO (25 nm)/IZO (50 nm)/GIZO (17 nm) layers. Here, the gallium-free sandwiched IZO layer has a lower bandgap ($\sim$2.9 eV) and longer Urbach tails[27,28]. The latter serves to enhance the optical absorption at longer wavelengths.

Figure 1a shows the top and cross-sectional views of the photosensor pixel, respectively, incorporating an inverted staggered switch-TFT and photo-TFT, both of which are integrated on the active matrix using the same fabrication process. The TFTs consist of SiO_x gate dielectric and passivation layers, a semiconductor tri-layer comprising GIZO (25 nm)/IZO (50 nm)/GIZO (17 nm), along with molybdenum metallization (see the bottom inset and Supporting Information S1). Here, the active channel is composed of nano-sized crystalline islands embedded within an amorphous

[1]Semiconductor Device Laboratory, Samsung Advanced Institute of Technology, Samsung Electronics Corporation, Yongin-Si, Gyeonggi-Do 446-712, Republic of Korea, [2]Analytical Science Group, Samsung Advanced Institute of Technology, Samsung Electronics Corporation, Yongin-Si, Gyeonggi-Do 446-712, Republic of Korea, [3]Engineering Department, Centre for Advanced Photonics and Electronics, Cambridge University, Cambridge CB3 0FA, UK, [4]London Centre for Nanotechnology, University College London, London WC1H 0AH, UK. *e-mail: sanghun1.jeon@samsung.com; ihsong@samsung.com.

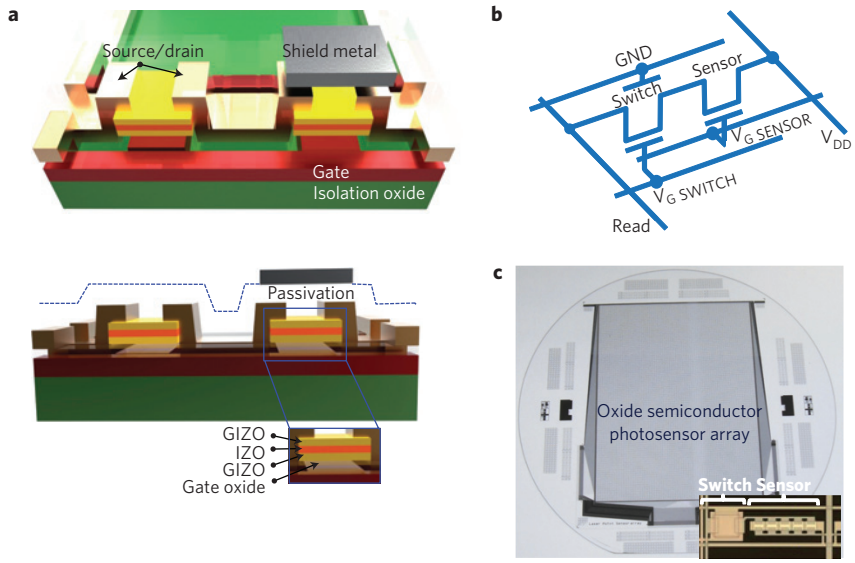

Figure 1 | The structure of an amorphous oxide semiconductor photosensor pixel comprising a gated three-terminal photosensor and a gated three-terminal switch. a, Schematic of a sensor pixel incorporating an inverted staggered switch-TFT and photo-TFT. The green region correspond to the display pixel. The inset at the bottom shows the cross-sectional view. **b**, The photosensor pixel circuit; the $V_{G\ SENSOR}$ terminal gives control over both the light sensitivity and PPC, and the $V_{G\ SWITCH}$ terminal performs the read-out operation. **c**, Photograph of the fully fabricated photosensor pixel array. The inset shows a photosensor composed of one photo-TFT and one switch-TFT.

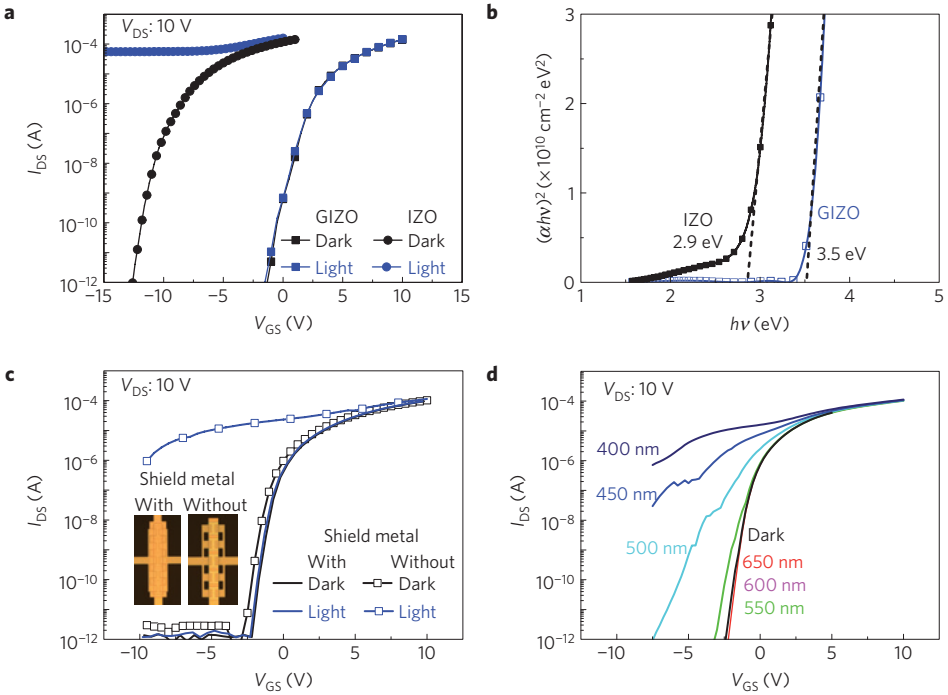

Figure 2 | Electrical, material and optical characteristics of IZO, GIZO, and GIZO/IZO/GIZO devices. a, Transfer characteristics of IZO and GIZO TFTs both in the dark and under illumination. Here, only IZO TFTs show light sensitivity. **b**, Tauc plot; $(\alpha h\nu)^2$ as a function of photon energy $h\nu$, where ν is the photon frequency, indicating the optical bandgap for IZO (2.9 eV) and GIZO (3.5 eV) layers. The larger Urbach tail in IZO, together with its lower optical bandgap, explains its greater light sensitivity. **c**, Transfer characteristics of GIZO/IZO/GIZO TFTs both with and without a top metal layer; the top metal layer effectively shields the channel from illumination. Inset: Micrograph of GIZO/IZO/GIZO TFTs both with and without a top metal layer. **d**, Transfer characteristics of GIZO/IZO/GIZO TFTs under exposure to 400, 450, 500, 550, 600 and 650 nm light with a power of ~100 μW cm^{-2}. The TFTs are sensitive to wavelengths shorter than 550 nm.

matrix (Supplementary Information S2 and S3). In this stacked structure, the GIZO layers were employed to allow adjustment of the threshold voltage (V_T) to a more positive value while protecting the thicker sandwiched IZO layer from damage during processing (Supplementary Information S2).

Figure 1b shows the photosensor pixel circuit and Fig. 1c shows the fabricated 192 × 256 photosensor array. Here, the switch-TFT and the photo-TFT have aspect ratios (W/L) of 50 μm/50 μm and 125 μm/10 μm, respectively. This yields an aperture ratio of 80%, indicating that a very large fraction of the sensor array

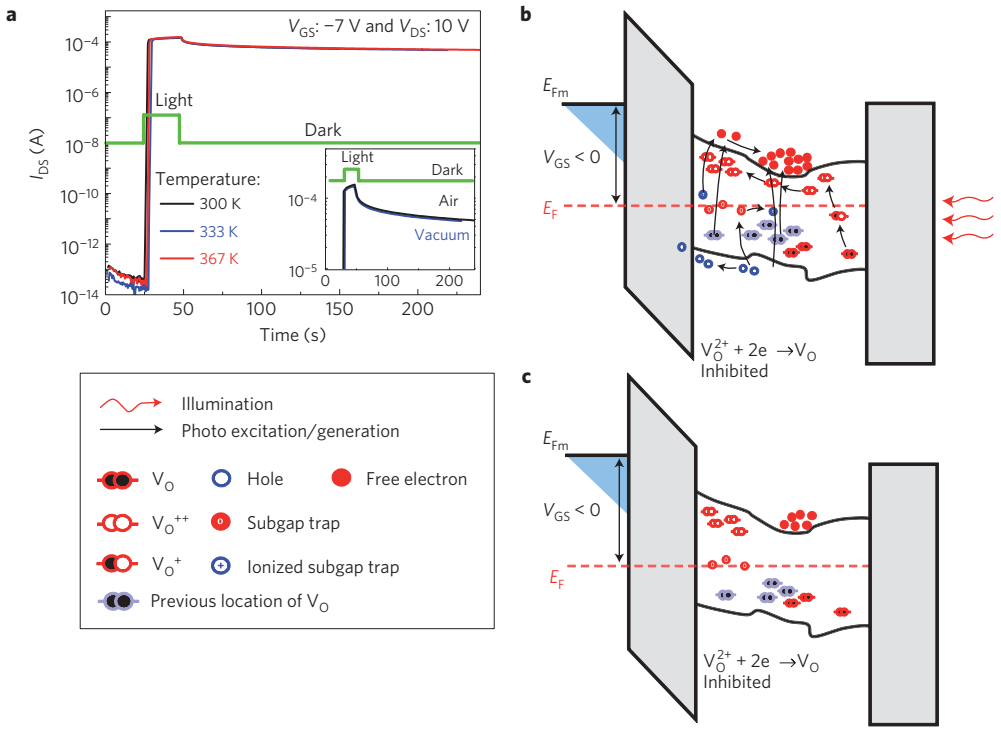

Figure 3 | PPC phenomenon of an oxide-based sensor device. a, Drain–source current as a function of time as the TFT is subjected to a light pulse (green) at substrate temperatures of 300, 333 and 367 K. The values of V_{GS} and V_{DS} are maintained at −7 and 10 V, respectively, during the measurements. Here, the photocurrent persists long after illumination has been removed. Inset: Drain–source current as a function of time as the TFT is subjected to a light pulse in air and under vacuum. The PPC remains even under vacuum. **b**, Schematic band diagram of the TFTs under a negative gate bias and light illumination; illumination empties the donor-like states while ionizing the oxygen vacancy sites, thus converting them from deep neutral states into shallow doubly-ionized donor states. At the same time, negative charges on the gate are compensated by positively charged oxygen vacancies, V_O^{2+}, leading to the formation of an un-depleted back channel, where photogenerated electrons are confined. **c**, Schematic band diagram of an oxide semiconductor TFT in the absence of light and under a negative gate bias. The negative gate bias confines V_O^{2+} to the front channel and electrons to the back hetero-interface, slowing the recombination of V_O^{2+} sites near the front interface and thus prolonging the PPC.

surface is transparent. In this pixel architecture, the photo-TFT is connected serially to the switch-TFT and to an off-panel read-out integrated circuit, allowing the photocurrent to be read, stored and subsequently visualized on a PC monitor.

Observations identify the IZO as the main light absorption layer. This is due to its enhanced electron–hole (e–h) pair generation from both subgap as well as band-to-band transitions. The in-dark and under-illumination transfer characteristics of a GIZO-only and an IZO-only TFT, both fabricated under similar deposition conditions as the TFTs in the sensor array, are compared in Fig. 2a. Note that only the IZO TFT exhibits light sensitivity. This can be explained based on the Tauc plot of the IZO and GIZO layers (Fig. 2b), determined using $\alpha t = -\ln(T/(1-R))$, where α is the absorption coefficient, t is the sample thickness, T transmittance, and R reflectance (see Fig. 2b; refs 27,28). Here, the addition of gallium is believed to suppress oxygen vacancy formation, increasing the optical bandgap while sharpening the Urbach tail and thus reducing the density of subgap defect states[27,28].

Figure 2c shows transfer characteristics of the photo-TFT and switch-TFT, which yield a field effect mobility μ_{FE} of 23 $cm^2\,V^{-1}s^{-1}$, V_T of −1.4 V, and sub-threshold slope (SS) of 300 mV per dec. Here, the photo-TFTs remain light sensitive whereas the switch-TFTs are shielded using a top molybdenum layer. In contrast to the two-terminal photosensor, the gated sensor presented here provides control over light sensitivity by enabling the gate-induced lowering of the Fermi level to deplete the channel. This raises the I_{photo}/I_{dark} ratio to ∼10^7, where I_{photo} is the photocurrent and I_{dark} is the dark current, under exposure to ∼100 μW cm^{-2} at $\lambda = 400$ nm, when the gate-to-source V_{GS} is set to −5 V. Furthermore, the λ-dependence of the photo-TFTs was measured by exposing them to 650, 600, 550, 500, 450 and 400 nm wavelength light at a power of ∼100 μW cm^{-2}. The photo-TFTs are sensitive only to wavelengths $\lambda < 550$ nm (Fig. 2d). Here, the increased absorption coefficient observed at shorter wavelengths leads to an increased photocurrent.

An important figure of merit for the photo-TFT is the threshold voltage stability under negative bias–light stress, which affects the key figures of merit such as photosensitivity, noise and lifetime during device operation. As seen in Supplementary Information S4, subjecting the photo-TFTs to 3 h of negative bias–temperature stress causes a manageable V_T shift of less than 2 V, estimated by tracking the changes in the gate voltage required to induce a current of $(W/L) \times 10$ nA. Here, the gate and drain stress voltages were −20 and 10 V, respectively, and the temperature was 60 °C. The negative shifts in the transfer characteristics shown in the inset can be attributed to bias-induced emptying of donor-like traps (neutral when occupied and positive when empty) near the interface, which act as localized trapped holes, thus raising the effective gate overdrive (V_{GS}–V_T). As shown in Fig. 3a, the photocurrent, measured using a Keithley 4200, rapidly increases by more than eight orders of magnitude on illumination, and persists long after the illumination has been removed. This PPC causes the active channel to act as though it is n-doped, lowering the threshold voltage to keep the photo-TFT always on.

We attribute the PPC primarily to the ionization of oxygen vacancy (V_O) sites. The inset of Fig. 3a shows that the PPC remains even under vacuum, albeit with a faster recovery rate. One potential explanation is that PPC in oxide semiconductors is due to light causing the surface oxygen species to desorb, raising

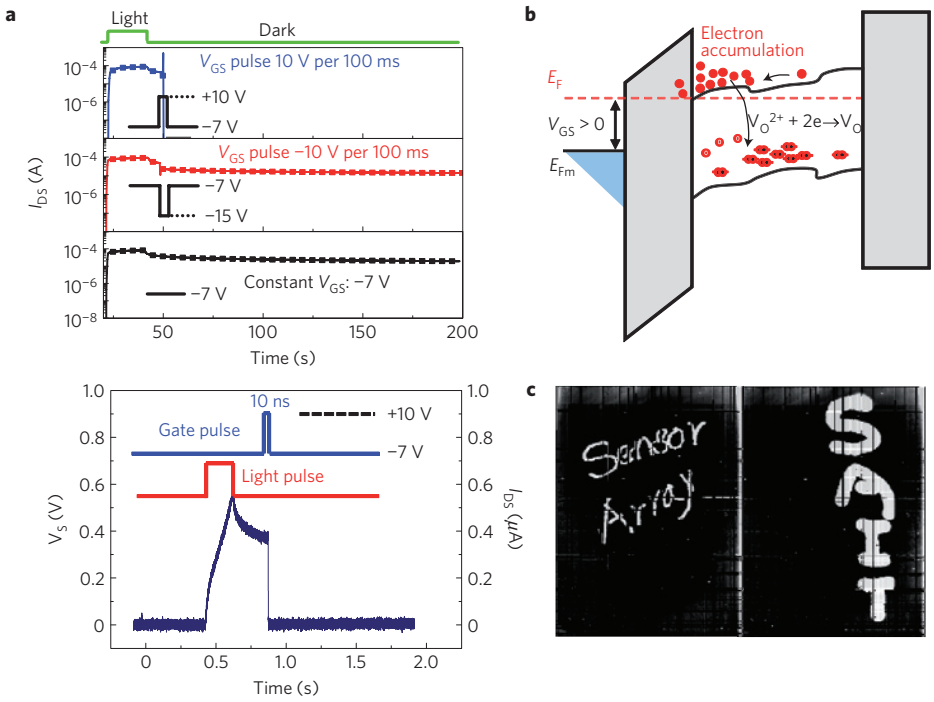

Figure 4 | Fermi-level control of oxide–semiconductor to eliminate the PPC phenomenon, and demonstration of a photosensor screen. a, Drain–source current as a function time when TFTs are subjected to light and/or gate bias pulses. Even after the illumination is stopped, the photocurrent persists. Only a positive gate pulse is effective in resetting the original dark state, that is a 10-ns positive gate voltage pulse leads to recovery from PPC. **b**, Schematic band diagram of an oxide TFT, conceptually depicting the positive-bias-assisted PPC recovery mechanism. A positive bias increases the electron concentration within the channel, accelerating the recombination of V_O^{2+} sites and hence recovery from PPC. **c**, Image visualized on a display; the words 'Sensor Array' are written using a green laser pointer held at a distance 30 cm from the display surface, and the letters 'SAIT' are written using a white LED pen held at a distance of 1–2 cm.

the photoconductivity[23,29], and that the subsequent re-adsorption of surface species then governs the slow decay in the dark. This mechanism (particularly pronounced in nanostructures with a high surface-to-volume ratio) can be ruled out here because the photo-TFTs considered are made of passivated thin films and the PPC remains under vacuum. Here, as proposed by Lany *et al.*[5] and Janotti *et al.*[30], illumination with $\lambda < 550$ nm is thought to ionize the deep, neutral V_O states to shallow donor states (V_O^{2+}), as depicted in the band diagrams in Fig. 3b (also presented in Supplementary Information S5). To provide mechanistic insights, various materials analyses were performed (depicted in Supplementary Information S6–S10). The outward relaxation of bonds surrounding the V_O sites then creates an energy barrier (~0.3 eV) against neutralization of V_O^{2+} sites, thus keeping the material in a state of high conductivity[5]. Consequently, the light-induced negative ΔV_T, and thus ΔI_{photo}, can be approximately described by assuming that PPC simply raises the flat-band Fermi level (E_{F0}) because of the increased electron doping concentration of the film. This increases the flat-band voltage but reduces the band bending required to turn on the channel. Thus, assuming that trap capacitance is much smaller than the insulator capacitance (C_i), ΔV_T can be estimated by:

$$\Delta V_T \approx -\left[\frac{qD_{it}}{C_i}\Delta E_{F0} + \frac{\Delta Q_{trap}}{C_i} + \frac{\Delta Q_T}{C_i}\right] \quad (1)$$

where D_{it} is the density of interface states, Q_{trap} the trapped charge inside or near the dielectric, and Q_T the gate-voltage induced charge density at threshold condition. Because illumination raises the photocurrent by many orders of magnitude, the density of ionized V_O sites can be taken as $\Delta n/2$, as each V_O^{2+} releases two electrons into the conduction band. Here, Δn is the density of photogenerated electrons. Therefore, ΔV_T can be defined in terms of the density of V_O^{2+} ($n_{V_O^{2+}}$), combining equation (1) with $\Delta E_{F0} = kT\ln(n_{V_O^{2+}}/n_o)$ (ref. 31):

$$\Delta V_T \approx -\left[\frac{qD_{it}kT}{C_i}\ln\left(\frac{n_{V_O^{2+}}}{n_o}\right) + \frac{\Delta Q_{trap}}{C_i} + \frac{\sqrt{2\varepsilon_S kT}}{C_i}\left(\sqrt{n_{V_O^{2+}}} - \sqrt{n_o}\right)\right] \quad (2)$$

where ε_S is permittivity of the channel layer and n_o the pre-illumination carrier concentration. Based on equations (1) and (2), the light-induced negative V_T shift can be decreased by reducing the density of V_O sites (which also enhance photosensitivity) while maintaining trap/interface conditions (D_{it} and Q_{trap}), by accelerating the recovery of V_O^{2+} sites and/or by deliberately trapping electrons inside or near the dielectric. The gated terminal, as we will see later, provides control over the latter two compensation techniques by enabling the manipulation of the position of the Fermi level.

In the results shown, the illumination was applied when the photo-TFT was subjected to a V_{GS} and drain-to-source voltage V_{DS} of −7 and 10 V, respectively. Here, V_{GS} is biased negatively to maximize the photocurrent gain and V_{DS} is positive to read out the data. This negative bias V_{GS} compounds the PPC by further reducing V_T (Fig. 3a). Consequently, it is the negative bias which seems to be the factor limiting the PPC decay, removing the expected temperature dependence of PPC recovery. Indeed, as seen in Fig. 3a, the estimated characteristic recovery time is of the order of days under this bias condition, apparently rendering these devices unusable as photosensors. This is due to the fact that the negative bias causes a physical separation of photogenerated electron–hole pairs by confining the electrons to the back channel, even after the illumination has stopped, as shown in Fig. 3c. As both the V_O^{2+} sites

and the holes photogenerated within the valence band are localized, physical confinement of the photogenerated electrons near the back channel further inhibits the recovery by slowing the reaction, $V_O^{2+} + 2e^- \rightarrow V_O$, and thus reduces V_T further (see equation (2)).

However, applying a positive gate voltage can overcome the adverse effects of PPC. As demonstrated in Fig. 4a, a 10-ns positive pulse (10 V; applied using, for example, an Agilent 81110A pulse generator, and measured using a Tektronix DPO 70604 oscilloscope) erases the PPC, enabling an operational scheme that manages the PPC in sensor arrays. As schematically depicted in Fig. 4b, this technique operates by raising the Fermi level to induce electron accumulation near the front channel, thereby accelerating the reaction, $V_O^{2+} + 2e^- \rightarrow V_O$, and hence recovery (see equation (2)). A further contributing mechanism to the accelerated recovery can be electron trapping inside or near the active channel/dielectric interface, which increases the V_T, as predicted by equation (1). Consequently, the optimal driving scheme interleaves both positive and negative pulses to help recover from PPC and discharge trapped electrons, respectively. The underlying PPC mechanism for oxide semiconductors in general follows the proposals by Lany *et al.*[5] and Janotti *et al.*[30], which we have applied to explain the photo-induced effects in our oxide system. Although the model seems to explain our experimental findings, it does not by any means rule out variations in the proposed model, nor does it dismiss possible alternative explanations.

Figure 4c demonstrates an all-oxide photosensor array prototype based on the bias-assisted PPC recovery scheme. Here, the words 'Sensor Array' were written using a green laser pointer held 30 cm in front of the panel, and the letters 'SAIT' were written with a white light LED pen held 1–2 cm in front of the display. The arrays have a response time of 25 μs, yielding a frame rate of 150 Hz (see Supplementary Visual Audio File).

In conclusion, we have demonstrated a gated photosensor array consisting of high-mobility GIZO/IZO/GIZO TFTs, whose materials system has been judiciously chosen to increase the light sensitivity by several orders of magnitude. The photo-TFTs, although stable under a negative bias–temperature stress, suffer from the adverse PPC effect, with recovery times on the scale of days. However, by applying short positive gate pulses, we are able to erase the PPC, enabling an operational scheme for managing both instability and PPC. The results presented here demonstrate the feasibility of transparent interactive active-matrix displays with embedded imaging that enable both touch and touch-free operation.

Received 6 June 2011; accepted 26 January 2012; published online 26 February 2012

References

1. Nomura, K. *et al.* Room-temperature fabrication of transparent flexible thin-film transistors using amorphous oxide semiconductors. *Nature* **432,** 488–492 (2004).
2. Fortunato, E., Pereira, L. & Barquinha, P. Oxide semiconductors: Order within the order. *Phil. Mag.* **89,** 2741–2758 (2009).
3. Robertson, J. Disorder, band offsets and dopability of transparent conducting oxides. *Thin Solid Films* **516,** 1419–1425 (2008).
4. Hoffman, R. L., Norris, B. J. & Wager, J. F. ZnO-based transparent thin-film transistors. *Appl. Phys. Lett.* **82,** 733–735 (2003).
5. Lany, S. & Zunger, A. Anion vacancies as a source of persistent photoconductivity in II–VI and chalcopyrite semiconductors. *Phys. Rev. B* **72,** 035215 (2005).
6. Jiang, H. X. & Lin, J. Y. Percolation transition of persistent photoconductivity in II–VI mixed crystals. *Phys. Rev. Lett.* **64,** 2547–2550 (1990).
7. Nomura, K. *et al.* Thin film transistor fabricated in single-crystalline transparent oxide semiconductor. *Science* **23,** 1269–1272 (2003).
8. Park, J. C. *et al.* Highly stable transparent amorphous oxide semiconductor thin film transistors having double stacked active layers. *Adv. Mater.* **22,** 5512–5516 (2010).
9. Jeon, S. *et al.* Nanometer-scale oxide thin film transistor with potential for high density image sensor applications. *ACS Appl. Mater. Int.* **3,** 1–6 (2011).
10. Lee, M-J. *et al.* Low temperature-grown transition metal oxide based storage materials and oxide transistors for high density non-volatile memory. *Adv. Funct. Mater.* **18,** 1587–1593 (2008).
11. Hosono, H. Ionic amorphous oxide semiconductors: Material design, carrier transport, and device application. *J. Non-Cryst. Solids* **352,** 851–858 (2006).
12. Park, K. *et al.* Transparent and photo-stable ZnO thin film transistors to drive an active matrix organic-light-emitting diode display panel. *Adv. Mater.* **21,** 678–682 (2009).
13. Liu, P-T., Chou, Y-T. & Teng, L-F. Charge pumping method for photosensor application by using amorphous indium–zinc oxide thin film transistors. *Appl. Phys. Lett.* **94,** 242101 (2009).
14. Janotti, A. & Van de Walle, C. G. Native point defects in ZnO. *Phys. Rev. B* **76,** 165202 (2007).
15. Oba, F., Togo, A., Tanaka, I., Paier, J. & Kresse, G. Defect energetics in ZnO: A hybrid Hartree–Fock density functional study. *Phys. Rev. B* **77,** 245202 (2008).
16. Feng, P. *et al.* Giant persistent photoconductivity in rough silicon nanomembranes. *Nano Lett.* **9,** 3453–3459 (2009).
17. Su, Y. K. *et al.* Ultraviolet ZnO nanorod photosensors. *Langmuir* **26,** 603–606 (2010).
18. Suehiro, J. *et al.* Dielectrophoretic fabrication and characterization of a ZnO nanowire-based UV photosensor. *Nanotechnology* **17,** 2567–2573 (2006).
19. Ryu, B., Noh, H-K., Choi, E-A. & Chang, K. J. O-vacancy as the origin of negative bias illumination stress instability in amorphous In–Ga–Zn–O thin film transistors. *Appl. Phys. Lett.* **97,** 022108 (2010).
20. Ghaffarzadeh, K. *et al.* Persistent photoconductivity in Hf–In–Zn–O thin film transistor. *Appl. Phys. Lett.* **97,** 143510 (2010).
21. Gorrn, P., Lehnhardt, M., Riedl, T. & Kowalsky, W. The influence of visible light on transparent zinc tin oxide thin film transistors. *Appl. Phys. Lett.* **91,** 193504 (2007).
22. Kamada, Y. *et al.* Reduction of photo-leakage current in ZnO thin film transistors with dual gate structure. *IEEE Electron Devices Lett.* **32,** 509–511 (2011).
23. Jin, Y., Wang, J., Sun, B., Blakeseley, B. C. & Greenham, N. C. Solution-processed ultraviolet photodetectors based on colloidal ZnO nanoparticles. *Nano Lett.* **8,** 1649–1653 (2008).
24. Soci, C. *et al.* ZnO nanowire UV photodetectors with high internal gain. *Nano Lett.* **7,** 1003–1009 (2007).
25. Li, L. *et al.* Electrical transport and high performance photoconductivity in individual ZrS_2 nanobelts. *Adv. Mater.* **22,** 4151–4156 (2010).
26. Xia, F., Mueller, T., Lin, Y-M., Valdes-Garcia, A. & Avouris, P. Ultrafast graphene photodetector. *Nature Nanotechnol.* **4,** 839–843 (2009).
27. Kamiya, T., Nomura, K., Hirano, M. & Hosono, H. Electronic structure of oxygen deficient amorphous oxide semiconductor a-InGaZnO: Optical analyses and first-principle calculations. *Phys. Status Solidi C* **5,** 3098–3100 (2008).
28. Nomura, K. *et al.* Subgap states in transparent amorphous oxide semiconductor, In–Ga–Zn–O, observed by bulk sensitive X-ray photoelectron spectroscopy. *Appl. Phys. Lett.* **92,** 202117 (2008).
29. Prades, J. *et al.* The effect of electron–hole separation on the photoconductivity of individual metal oxide nanowires. *Nanotechnology* **18,** 465501 (2008).
30. Janotti, A. & Van de Walle, C. G. Oxygen vacancies in ZnO. *Appl. Phys. Lett.* **87,** 122102 (2005).
31. Kuo, Y. *Thin Film Transistors: Materials and Processes Vol. 1* (Kluwer Academic, 2003).

Acknowledgements

The authors are grateful to SAIT colleagues Y. K. Cha, K. J. Park and C. Y. Moon for assistance with the experiments, and S. Heo and J. Lee for X-ray photoelectron spectroscopy analysis.

Author contributions

S.J., S-E.A. and I.S. designed this work. S.J. and A.N. prepared the manuscript. S.J., S-E.A. and I.S. carried out the experiment and electrical analysis. E-h.L. performed transmission electron microscopy analysis. S.L. worked on drawing the energy band diagram and deriving the equations. A.N. and J.R. contributed to analysis and interpretation of results relevant to persistent photoconductivity and photoconductive gain. All authors discussed the results and implications and commented on the manuscript at all stages.

Additional information

The authors declare no competing financial interests. Supplementary information accompanies this paper on www.nature.com/naturematerials. Reprints and permissions information is available online at www.nature.com/reprints. Correspondence and requests for materials should be addressed to S.J. or I.S.